Green Chemistry

PAPER

View Article Online
View Journal | View Issue

Check for updates

Cite this: *Green Chem.*, 2024, **26**, 2599

Stabilization of Cu^+ sites by amorphous Al_2O_3 to enhance electrochemical CO_2 reduction to C_{2+} products†

Hailian Cheng,[a,b] Shuaiqiang Jia,*[a,b] Jiapeng Jiao,[a,b] Xiao Chen,[a,b] Ting Deng,[a,b] Cheng Xue,[a,b] Mengke Dong,[a,b] Jianrong Zeng,[d] Chunjun Chen,[a,b] Haihong Wu,*[a,b] Mingyuan He[a,b] and Buxing Han*[a,b,c]

Received 18th November 2023,
Accepted 12th January 2024

DOI: 10.1039/d3gc04492k

rsc.li/greenchem

Catalytic conversion of CO_2 to produce fuels and chemicals is of great importance, and the electrocatalytic CO_2 reduction reaction (eCO_2RR) is considered one of the most attractive pathways. Multi-carbon (C_{2+}) products are more desirable in many cases. To date, Cu-based catalysts, especially Cu^+ sites, have been found to be the most efficient for the production of C_{2+} products. However, the retention of Cu^+ sites at high cathodic potentials in the eCO_2RR remains a great challenge. In this study, we designed and synthesized CuAl-oxide-derived (Cu_xAl_y-OD, *x* and *y* are the mass percentages of Cu and Al) catalysts for the eCO_2RR to C_{2+} products. During the eCO_2RR process, the predominant Cu species changed to Cu^+, and the resulting electrocatalyst showed a high faradaic efficiency (FE) of 81.6% for C_{2+} products in alkaline aqueous solutions. Experimental studies showed that the presence of a stable amorphous Al_2O_3 phase stabilized the Cu^+ sites by oxidation state control, leading to high selectivity and activity for the production of C_{2+} products. This work provides a strategy for improving the stability of Cu^+ in the catalyst to enhance the performance of the eCO_2RR.

Published on 15 de gener 2024. Downloaded on 31/5/2026 0:39:09.

Introduction

The catalytic conversion of CO_2 to produce fuels and chemicals is of great importance, as it ameliorates both environmental concerns and the energy crisis.[1–4] The electrocatalytic CO_2 reduction reaction (eCO_2RR), in particular, is considered one of the most attractive pathways for carbon cycle rebalancing due to its mild operating conditions, ease of operation, product adjustment, and potential for synergy with renewable energy sources.[5–8] To date, Cu-based catalysts have been found to be the most efficient for the production of multi-carbon (C_{2+}) hydrocarbons and oxygenated products.[9–11] However, Cu-based catalysts still have certain limitations, including poor stability,[12] poor selectivity for specific products, and competition from the hydrogen evolution reaction (HER).[13]

To address these challenges, various strategies have been employed to improve the selectivity, activity, and stability of Cu-based catalysts for the eCO_2RR, including surface treatment of Cu electrodes,[14–16] alloying,[17–20] doping of other metal elements to modulate the electronic structure[21–23] and formation of coordination compounds.[24–29] It is noteworthy that in order to stabilize the active sites of Cu catalysts, researchers have attempted to use metal–organic frameworks (MOFs) with specially designed ligands to achieve the stabilization of the Cu^{2+} site,[16,30] but unfortunately, the Cu-MOF catalysts reported so far did not continuously stabilize Cu^{2+} during electrolysis but were electrochemically reduced to Cu^0.[31] At the same time, it has also been reported that Cu^{2+} is incorporated into oxide matrices to form Cu–M–O solid solutions in order to stabilize Cu^{2+} during the eCO_2RR process.[32] However, most of the target products obtained by the above strategy of stabilizing Cu^{2+} active sites were methane or other monocarbon products. Therefore, the development of catalysts with stabilized Cu^+ sites for enhancing the dimerization of the reaction intermediate *CO and hence the selectivity of higher value-added C_{2+} products remains challenging.

Here, we prepared a catalyst capable of stabilizing the Cu^+ site in the eCO_2RR process by introducing the metal Al to form

[a]*Shanghai Key Laboratory of Green Chemistry and Chemical Processes, State Key Laboratory of Petroleum Molecular & Process Engineering, School of Chemistry and Molecular Engineering, East China Normal University, Shanghai, 200062, China. E-mail: sqjia@chem.ecnu.edu.cn, hhwu@chem.ecnu.edu.cn, hanbx@iccas.ac.cn*
[b]*Institute of Eco-Chongming, 20 Cuiniao Road, Chenjia Town, Chongming District, Shanghai, 202162, China*
[c]*Beijing National Laboratory for Molecular Sciences, CAS Key Laboratory of Colloid and Interface and Thermodynamics, CAS Research/Education Center for Excellence in Molecular Sciences, Center for Carbon Neutral Chemistry, Institute of Chemistry, Chinese Academy of Sciences, Beijing, 100190, China*
[d]*Shanghai Synchrotron Radiation Facility, Shanghai Advanced Research Institute, Chinese Academy of Sciences, 201204, China*

†Electronic supplementary information (ESI) available. See DOI: https://doi.org/10.1039/d3gc04492k

Published on 15 de gener 2024. Downloaded on 31/5/2026 0:39:09.

a Cu_xAl_y-OD nanosheet catalyst. Remarkably, using the $Cu_{100}Al_{7.88}$-OD catalyst as an electrode in a flow cell with a 1 M KOH electrolyte, we obtained a total current density of 692.6 mA cm^{-2} with a faradaic efficiency (FE) of 81.6% for C_{2+} products, which was twice as high as that of FE_{C2+} over a pure CuO-OD catalyst. *In situ* Raman spectroscopy measurements and X-ray absorption spectroscopy (XAS) experiments showed that the broadened orbital in interfacial Al_2O_3 offers a lower orbital for extra electrons than Cu^+, which can effectively retain nearby Cu^+, and the highly active Cu^+ sites significantly enhance C–C coupling, improving the selectivity and activity of the eCO_2RR to C_{2+} products.

Results and discussion

The synthesis of Cu_xAl_y-OD electrodes involves a two-step process (Fig. 1a). First, the Cu_xAl_y-oxide (named Cu_xAl_y-Ox) catalysts were prepared by the co-precipitation of $CuCl_2{\cdot}2H_2O$ and $AlCl_3{\cdot}6H_2O$ salts (the details of the synthesis method are provided in the ESI†), and then transferred to a hydrothermal reactor and placed in a 100 °C oven for 18 h. Further Cu_xAl_y-OD electrodes were obtained by the redox reaction cyclic voltammetry (CV) technique. The mass percentages of Cu and Al in the as-synthesized Cu_xAl_y-Ox catalysts were determined by inductively coupled plasma optical emission spectroscopy (ICP-OES) (Table S1†). The $Cu_{100}Al_{7.88}$-Ox catalyst was used as a representative example. Scanning electron microscopy (SEM) and transmission electron microscopy (TEM) images showed that $Cu_{100}Al_{7.88}$-Ox exhibited a two-dimensional nanosheet morphology along with a rough edge structure (Fig. 1b and c). According to the ESI Fig. S1,† with the increase of Al doping, the morphology of the catalyst changed from a two-dimensional nanosheet structure to a flower-like structure. The high-resolution transmission electron microscopy (HRTEM) image (Fig. 1d) showed that the lattice fringes in the $Cu_{100}Al_{7.88}$-Ox catalyst were 0.250 nm and 0.274 nm, corresponding to the distance of the (111) and (110) planes of CuO, respectively.[33,34] It is noteworthy that no lattice fringes belonging to Al were found in HRTEM images, which may be because Al_2O_3 in the catalyst was an amorphous physical phase (Fig. S2 and S3†). Meanwhile, from the energy-dispersive X-ray spectroscopy (EDS) elemental mapping images (Fig. 1e), Cu, Al, and O were uniformly distributed in the $Cu_{100}Al_{7.88}$-Ox catalyst.

The electronic and chemical structures of the as-synthesized catalysts were characterized by different methods. The X-ray diffraction (XRD) patterns of the Cu_xAl_y catalysts before (Cu_xAl_y-Ox) and after CV activation (Cu_xAl_y-OD) are shown in Fig. 2a and b. It can be seen that before CV activation, the Cu phase of all catalysts was only CuO (JCPDS#48-1548). However, after CV activation the pure CuO catalyst changed into Cu^0,

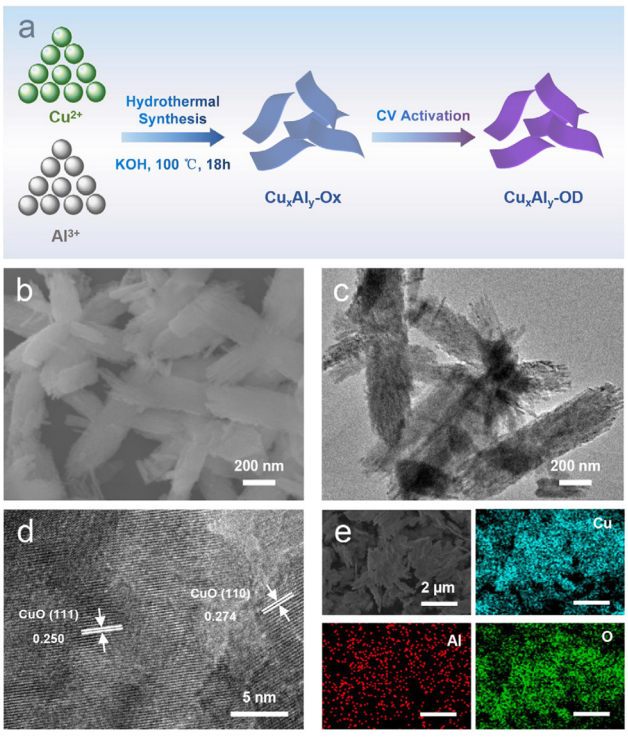

Fig. 1 Preparation and characterization of catalysts. (a) Schematic illustration of the process to prepare Cu_xAl_y-Ox catalysts. (b) SEM, (c) TEM, (d) HRTEM, and (e) EDS elemental mapping images of the $Cu_{100}Al_{7.88}$-Ox catalyst.

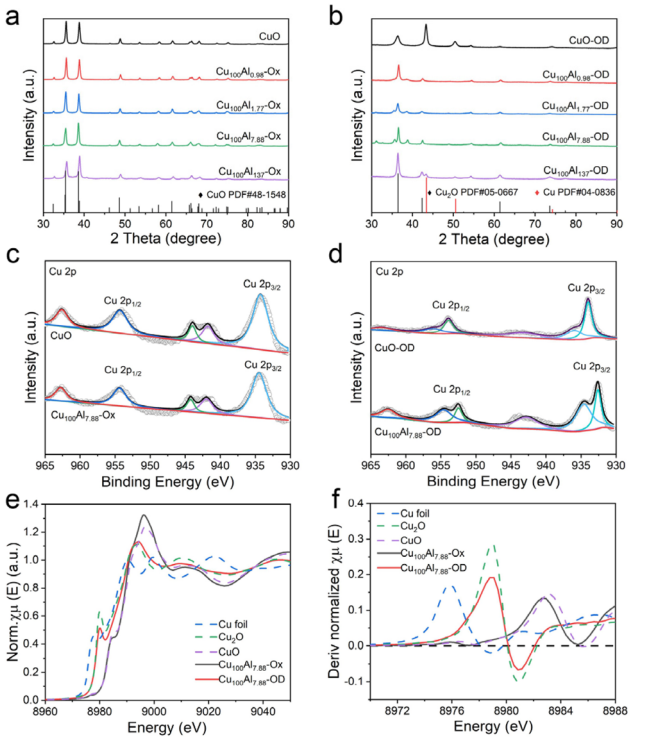

Fig. 2 XRD patterns of CuO and Cu_xAl_y-Ox catalysts (a) before and (b) after CV activation in a CO_2-saturated 1 M KOH electrolyte. Cu 2p XPS spectra of CuO and $Cu_{100}Al_{7.88}$-Ox catalysts (c) before CV activation and (d) after CV activation in a CO_2-saturated 1 M KOH electrolyte. (e) Normalized Cu K-edge XANES spectra and (f) derivative normalized spectra of different catalysts. For comparison, reference spectra from a Cu foil, Cu_2O, and CuO are also shown.

This journal is © The Royal Society of Chemistry 2024

Published on 15 de gener 2024. Downloaded on 31/5/2026 0:39:09.

whereas the Cu_xAl_y-OD catalyst was Cu_2O (JCPDS#05-0667). It is noteworthy that we did not find the diffraction peaks of Al in the XRD pattern, probably due to the insufficient crystallinity of Al_2O_3 in the catalysts prepared by this method, which existed as an amorphous phase.[35] X-ray photoelectron spectroscopy (XPS) experiments were used to gain insight into the electronic interaction between Cu and Al as well as the surface chemical states of each element in $Cu_{100}Al_{7.88}$-Ox and $Cu_{100}Al_{7.88}$-OD catalysts. Fig. 2c shows that the valence state of Cu in both CuO and $Cu_{100}Al_{7.88}$-Ox catalysts is Cu^{2+} accompanied by strong satellite peaks. After CV activation (Fig. 2d), the CuO electrode was easily reduced to Cu^0 in the catalyst without Al doping, while Cu_xAl_y-OD mostly retained Cu^+. The XPS spectra of Al 2p showed that Al was present in the physical phase of Al_2O_3 both before and after the activation of the $Cu_{100}Al_{7.88}$-Ox catalyst (Fig. S4†). Combined with the XRD and XPS results, it can be observed that the CuO catalyst was reduced to metallic Cu^0, which proved that Cu^{2+} without oxidation state control protection can be easily reduced, further illustrating the importance of amorphous Al_2O_3 in stabilizing the Cu^+ site.

To further investigate the chemical state and electronic structure of Cu in the $Cu_{100}Al_{7.88}$-Ox and $Cu_{100}Al_{7.88}$-OD catalysts, synchrotron X-ray absorption spectroscopy (XAS) was performed on the catalysts prepared in this work, and the spectra of Cu foil, Cu_2O and CuO as references were obtained. As shown in Fig. 2e, normalized X-ray absorption near edge structure spectra (XANES) of the Cu K-edge showed that the Cu species in $Cu_{100}Al_{7.88}$-Ox exhibited an oxidized state (+2), the same as the CuO reference sample, whereas the Cu species in $Cu_{100}Al_{7.88}$-OD exhibited the same +1 valence state as the Cu_2O reference sample. Moreover, this was further confirmed by the corresponding derivative normalized spectra (Fig. 2f) and the *k*3-weighted Cu K edge Fourier-transform extended X-ray absorption fine structure (FT-EXAFS) spectra (Fig. S5†), which indicated that the presence of amorphous Al_2O_3 could stabilize Cu^+ to prevent its reduction to Cu^0. This is consistent with the results of the XPS and XRD analyses.

The eCO_2RR catalytic performances of Cu_xAl_y-OD catalysts were tested in a flow cell. 1 M KOH was used as the electrolyte, and the catalysts were loaded onto a gas diffusion layer (GDL). Gaseous products were probed and quantified during the eCO_2RR using gas chromatography (GC) and liquid products were examined after the completion of the electrochemical reaction *via* ^1H nuclear magnetic resonance (NMR). The linear sweep voltammetry (LSV) curves were measured in CO_2- and Ar-saturated 1 M KOH electrolytes, the $Cu_{100}Al_{7.88}$-OD electrode exhibited a higher current density in the CO_2-saturated electrolyte compared to the results in the Ar-saturated electrolyte, indicating the occurrence of an eCO_2RR on the $Cu_{100}Al_{7.88}$-OD electrode (Fig. 3a). We tested all the Cu_xAl_y-OD and CuO catalysts, including CuO-OD, $Cu_{100}Al_{0.98}$-OD, $Cu_{100}Al_{1.77}$-OD, $Cu_{100}Al_{7.88}$-OD, and $Cu_{100}Al_{137}$-OD, and compared their eCO_2RR performances. As shown in Fig. 3b, gaseous products (H_2, CO, CH_4, and C_2H_4) and liquid products (HCOOH, CH_3COOH, CH_3CH_2OH (EtOH), and $CH_3CH_2CH_2OH$ (PrOH))

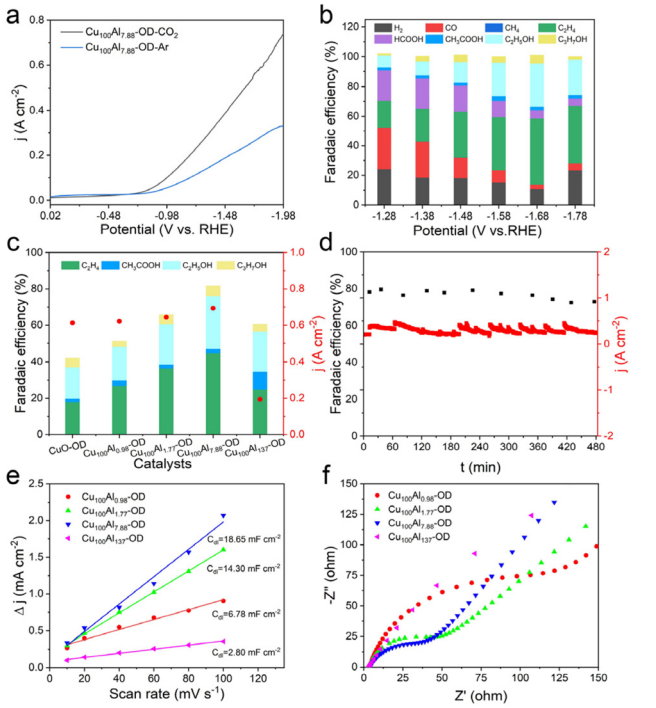

Fig. 3 Electrochemical performances of the Cu_xAl_y-OD catalyst. (a) LSV curves for $Cu_{100}Al_{7.88}$-OD in CO_2-saturated and Ar-saturated 1 M KOH electrolytes. (b) FE of the products over $Cu_{100}Al_{7.88}$-OD at different applied potentials. (c) FE_{C2+} and total current densities over Cu_xAl_y-OD at −1.68 V *vs.* RHE. (d) Electrochemical stability test of the $Cu_{100}Al_{7.88}$-OD electrode at −1.68 V *vs.* RHE in a flow cell. (e) Comparison of double-layer capacitance in a 1 M KOH electrolyte with Cu_xAl_y-OD. (f) Nyquist plots of Cu_xAl_y-OD in the 1 M KOH electrolyte. Data were obtained at ambient temperature and pressure with a CO_2 stream of 20 sccm.

were detected in the present catalytic system. According to the product distribution, the decreasing FE of H_2 and increasing FE of carbon products become obvious after Al doping into Cu catalysts. At a potential of −1.68 V *vs.* RHE, the FE of C_{2+} products over the $Cu_{100}Al_{7.88}$-OD electrode could reach 81.6% with a current density as high as 692.6 mA cm^{-2}, in which the partial current density of C_{2+} products could reach 565.2 mA cm^{-2} (Fig. S6†). The catalyst maintained a high C_{2+} yield as the applied potential increased. In contrast, pure CuO catalysts showed a maximum FE_{C2+} of only 41.8% compared to a potential of −1.68 V *vs.* RHE, and produced more H_2 and C_1 products, respectively. Fig. 3c shows the FE_{C2+} and j_{total} over different Cu_xAl_y-OD electrodes at −1.68 V *vs.* RHE, and it was found that the amount of Al doping was crucial for the selectivity of the C_{2+} product. A comparison of the electrocatalytic performances of the catalysts with different Cu/Al mass ratios revealed that the C_{2+} product exhibited good FE and partial current density at the $Cu_{100}Al_{7.88}$-OD electrode (Fig. S7–S10†). In addition to catalytic activity, stability is also one of the important criteria for evaluating catalyst performance. Subsequently, we conducted a stability test in a flow cell (Fig. 3d), in which the current density of the catalyst and FE_{C2+}

Published on 15 de gener 2024. Downloaded on 31/5/2026 0:39:09.

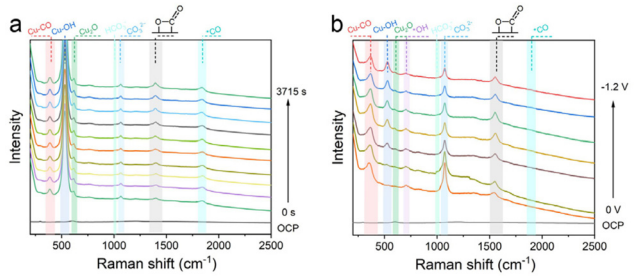

Fig. 4 *In situ* Raman spectra of (a) the $Cu_{100}Al_{7.88}$-OD electrode at −1.68 V *vs.* RHE with different reaction times during the eCO_2RR in a 0.5 M KOH electrolyte and (b) the $Cu_{100}Al_{7.88}$-OD electrode at various potentials during the eCO_2RR in a 0.5 M KOH electrolyte. All potentials are given *vs.* RHE.

remained unchanged after 8 h of electrolysis at −1.68 V *vs.* RHE, indicating that $Cu_{100}Al_{7.88}$-OD had a good stability for the eCO_2RR.

To explore the reasons for the excellent performance of the $Cu_{100}Al_{7.88}$-OD electrode, electrochemically active surface area (ECSA) and electrochemical impedance spectra (EIS) of Cu_xAl_y-OD electrodes were analyzed. The ECSA of the catalyst was then estimated through the electrochemical double-layer capacitance (C_{dl}) measurements. The CV curves with various scan rates in the non-faradaic region were recorded. As shown in Fig. 3e, the linear slopes show that the C_{dl} value for the $Cu_{100}Al_{7.88}$-OD electrode (18.65 mF cm^{-2}) is larger than those of the other catalysts, which demonstrates that doping of a suitable amount of Al can generate more active sites than the pure Cu catalyst. The EIS was also carried out to probe the effect of the metal ratios of the catalysts on the charge transport kinetics at the open circuit potential (OCP). It showed that the charge transfer resistance of the $Cu_{100}Al_{7.88}$-OD electrode was lower than that of other catalysts, indicating a favorable kinetics toward the eCO_2RR (Fig. 3f).[36]

To gain insight into characterizing both the structural evolution of catalyst surfaces and reaction intermediates at electrode/electrolyte interfaces during electrochemical reactions, *in situ* Raman spectroscopy was used to monitor the change of interfacial species and highly active sites of the $Cu_{100}Al_{7.88}$-OD electrode under different electrolysis times and potentials (Fig. 4). As shown in Fig. 4a, after prolonged electrolysis, the $Cu_{100}Al_{7.88}$-OD electrode showed a Raman peak at 620 cm^{-1}, which was attributed to Cu_2O.[37] This absorption peak corresponds to the peak at this location under OCP conditions and remains stable for more than 3000 s of continuous electrolysis, indicating that the Cu^+ site is stable during the eCO_2RR. The *in situ* Raman results demonstrate that the broadened orbital in interfacial amorphous Al_2O_3 offers a lower orbital for extra electrons than Cu^+, which can effectively retain nearby Cu^+.[38,39] It is worth noting that the catalyst was not exposed to ambient air during the Raman test, so the Cu^+ site was generated after CV activation and remained stable during the eCO_2RR process. The retention of the band at around 530 cm^{-1} for Cu-OH can be explained by the increase of the local pH near the catalyst surface at high reaction potentials (−1.68 V *vs.* RHE).[40] Interestingly, the Raman peaks at 1330 cm^{-1} belong to the CO_2^- in-stretching vibrations, which confirms the first intermediate during the eCO_2RR over the $Cu_{100}Al_{7.88}$-OD electrode.[41] The peaks around 1880 cm^{-1} are assigned to the C≡O stretching vibrations. Further investigation of the mechanism of the C_{2+} products from the $Cu_{100}Al_{7.88}$-OD electrode is very interesting. In particular, the peaks located in the range of 1800–2000 cm^{-1} are associated with the bridge site of *CO absorption (*CO_{bridge}), which can favor *CO–CO coupling.[42]

The *in situ* Raman spectra of the $Cu_{100}Al_{7.88}$-OD electrode at various potentials are shown in Fig. 4b; a Raman peak at 1012 cm^{-1} (representing a small amount of bicarbonate) and a Raman peak at 1068 cm^{-1} (representing carbonate) were detected in the $Cu_{100}Al_{7.88}$-OD electrode. According to previous studies, the density of localized proton donors near the catalyst surface can be estimated from the ratio of HCO_3^-/CO_3^{2-}.[43] As the applied potential decreases, the HCO_3^-/CO_3^{2-} ratio increases, indicating a decrease in proton donors near the $Cu_{100}Al_{7.88}$-OD electrode surface. These alkaline conditions promote the formation of C_{2+} products, which is consistent with our electrochemical results (Fig. 3c).[44,45]

Conclusions

In summary, we have proposed a method to stabilize the Cu^+ oxidation state with a suitable amount of Al_2O_3, and the catalyst can promote CO_2 electroreduction to C_{2+} products with high catalytic activity, selectivity, and stability. Combined *in situ* spectroscopic and electrochemical measurements indicate that Cu^+ stabilized by the amorphous Al_2O_3 enhances the adsorption stability of the *CO intermediate, which in turn promotes its further dimerization (C–C coupling) and thus significantly improves the selectivity for C_{2+} products. This discovery effectively solves the stability problem of Cu-based catalysts for the eCO_2RR and provides an effective way to design low-cost, energy-efficient catalysts.

Author contributions

H. L. C., S. Q. J., H. H. W. and B. X. H. proposed the project, designed the experiments, and wrote the manuscript. H. L. C. and S. Q. J. performed most of the experiments and analyzed the experimental data. J. P. J., X. C., T. D., C. X. M. K. D. and C. J. C. provided help in materials synthesis and characterization. H. L. C., S. Q. J., X. C. and J. R. Z. conducted XAS measurements and analyzed the results. H. H. W., M. Y. H. and B. X. H. co-supervised the whole project. All authors discussed the results and commented on the manuscript.

This journal is © The Royal Society of Chemistry 2024

Published on 15 de gener 2024. Downloaded on 31/5/2026 0:39:09.

Conflicts of interest

There are no conflicts to declare.

Acknowledgements

The work was supported by the National Key R&D Program of China (2023YFA1507901, 2020YFA0710201), the National Natural Science Foundation of China (22003070, 22293015, 22121002), the China Postdoctoral Science Foundation (2023M731096), and the Research Funds of Happiness Flower ECNU (2020ST2203). We thank the staff of beamline BL13SSW at Shanghai Synchrotron Radiation Facility for the support for the experiments of *in situ* XAS measurements.

References

1 R. E. Sharwood, *Science*, 2022, **378**, 137–138.
2 Z. Zhang, T. N. Borhani and A. G. Olabi, *Energy*, 2020, **205**, 118057.
3 M. E. Chu, C. J. Chen, Y. H. Wu, X. P. Yan, S. Q. Jia, R. T. Feng, H. H. Wu, M. Y. He and B. X. Han, *Green Energy Environ.*, 2022, **7**, 792–798.
4 S. Jia, Q. Zhu, M. Chu, S. Han, R. Feng, J. Zhai, W. Xia, M. He, H. Wu and B. Han, *Angew. Chem., Int. Ed.*, 2021, **60**, 10977.
5 G. Zhang, S. D. Straub, L. Shen, Y. Hermans, P. Schmatz, A. M. Reichert, J. P. Hofmann, I. Katsounaros and B. J. M. Etzold, *Angew. Chem., Int. Ed.*, 2020, **59**, 18095–18102.
6 X. X. Chang, M. He, Q. Lu and B. J. Xu, *Sci. China: Chem.*, 2023, **66**, 96–106.
7 S. Ma, M. Sadakiyo, R. Luo, M. Heima, M. Yamauchi and P. J. A. Kenis, *J. Power Sources*, 2016, **301**, 219–228.
8 D. Yang, X. Liu, Y. H. Dai, Y. Zhu and Y. H. Yang, *Chem. J. Chin. Univ.*, 2022, **43**, 20220198.
9 A. R. Woldu, Z. Huang, P. Zhao, L. Hu and D. Astruc, *Coord. Chem. Rev.*, 2022, **454**, 214340.
10 T. R. Wei, S. S. Zhang, Q. Liu, Y. Qiu, J. Luo and X. J. Liu, *Acta Phys.-Chim. Sin.*, 2023, **39**, 2207026.
11 L. Xu, J. Feng, L. Wu, X. Song, X. Tan, L. Zhang, X. Ma, S. Jia, J. Du, A. Chen, X. Sun and B. Han, *Green Chem.*, 2023, **25**, 1326–1331.
12 H. Zhang, C. He, S. Han, Z. Du, L. Wang, Q. Yun, W. Cao, B. Zhang, Y. Tian and Q. Lu, *Chin. Chem. Lett.*, 2022, **33**, 3641–3649.
13 K. Jiang, Y. Huang, G. Zeng, F. M. Toma, W. A. Goddard III and A. T. Bell, *ACS Energy Lett.*, 2020, **5**, 1206–1214.
14 O. Christensen, S. Zhao, Z. Sun, A. Bagger, J. V. Lauritsen, S. U. Pedersen, K. Daasbjerg and J. Rossmeisl, *ACS Catal.*, 2022, **12**, 15737–15749.
15 Z. Xin, Z. Yuan, J. Liu, X. Wang, K. Shen, Y. Chen and Y.-Q. Lan, *Chin. Chem. Lett.*, 2023, **34**, 107458.
16 S. J. Kang, J. H. Won, H. Choi, W. Sim, M. K. Kim, S. Sultan, Y. Kwon and H. M. Jeong, *J. Energy Chem.*, 2022, **66**, 68–73.
17 C. Choi, J. Cai, C. Lee, H. M. Lee, M. Xu and Y. Huang, *Nano Res.*, 2021, **14**, 3497–3501.
18 Y. Xu, C. Li, Y. Xiao, C. Wu, Y. Li, Y. Li, J. Han, Q. Liu and J. He, *ACS Appl. Mater. Interfaces*, 2022, **14**, 11567–11574.
19 X. Zhang, Y. Zhou, H. Zhang, H. Li, K. Liu, H. Li, H. Pan, J. Hu, J. Fu, S. Chen and M. Liu, *J. Energy Chem.*, 2021, **63**, 625–632.
20 Y. Ji and G. Zheng, *Sci. China: Chem.*, 2021, **64**, 1111–1112.
21 Z. Zhao, X. Li, J. Wang, X. Lv and H. B. Wu, *J. CO_2 Util.*, 2021, **54**, 101741.
22 J. Chen, X. Wei, R. Cai, J. Ren, M. Ju, X. Lu, X. Long and S. Yang, *ACS Mater. Lett.*, 2022, **4**, 497–504.
23 Z. Zhang, H. Tian, L. Bian, S. Liu, Y. Liu and Z. Wang, *J. Energy Chem.*, 2023, **83**, 90–97.
24 J. Wang, H. Tan, Y. Zhu, H. Chu and H. Chen, *Angew. Chem., Int. Ed.*, 2021, **60**, 17254–17267.
25 T. C. Chou, C. C. Chang, H. L. Yu, W. Y. Yu, C. L. Dong, J. J. Velasco-Vélez, C. H. Chuang, L. C. Chen, J. F. Lee, J. M. Chen and H. L. Wu, *J. Am. Chem. Soc.*, 2020, **142**, 2857–2867.
26 Z. Wu, F. Gao and M. Gao, *Energy Environ. Sci.*, 2021, **14**, 1121–1139.
27 H. Xiao, W. A. Goddard 3rd, T. Cheng and Y. Liu, *Proc. Natl. Acad. Sci. U. S. A.*, 2017, **114**, 6685–6688.
28 R. M. Arán-Ais, F. Scholten, S. Kunze, R. Rizo and B. Roldan Cuenya, *Nat. Energy*, 2020, **5**, 317–325.
29 X. Yuan, S. Chen, D. Cheng, L. Li, W. Zhu, D. Zhong, Z. Zhao, J. Li, T. Wang and J. Gong, *Angew. Chem., Int. Ed.*, 2021, **60**, 15344–15347.
30 L. Majidi, A. Ahmadiparidari, N. Shan, S. N. Misal, K. Kumar, Z. Huang, S. Rastegar, Z. Hemmat, X. Zou, P. Zapol, J. Cabana, L. A. Curtiss and A. Salehi-Khojin, *Adv. Mater.*, 2021, **33**, 2004393.
31 I. Merino-Garcia, J. Albo, J. Solla-Gullón, V. Montiel and A. Irabien, *J. CO_2 Util.*, 2019, **31**, 135–142.
32 X. Zhou, J. Shan, L. Chen, B. Y. Xia, T. Ling, J. Duan, Y. Jiao, Y. Zheng and S. Qiao, *J. Am. Chem. Soc.*, 2022, **144**, 2079–2084.
33 J. Jang, K. Lee, H. Shin, H. S. Lee, B.-H. Lee, J. Jeong, J. Kim, W. Hwang, S. Park, M. S. Bootharaju, S. Back, J. Shim, J. H. Kim, T. Hyeon and Y. Sung, *J. Mater. Chem. A*, 2023, **11**, 19066–19073.
34 X. Wang, K. Klingan, M. Klingenhof, T. Möller, J. Ferreira de Araújo, I. Martens, A. Bagger, S. Jiang, J. Rossmeisl, H. Dau and P. Strasser, *Nat. Commun.*, 2021, **12**, 794.
35 S. Rasul, D. H. Anjum, A. Jedidi, Y. Minenkov, L. Cavallo and K. Takanabe, *Angew. Chem., Int. Ed.*, 2015, **54**, 2146–2150.
36 T. N. Nguyen, Z. Chen, A. S. Zeraati, H. S. Shiran, S. M. Sadaf, M. G. Kibria, E. H. Sargent and C. T. Dinh, *J. Am. Chem. Soc.*, 2022, **144**, 13254–13265.
37 H. Li, P. Wei, D. Gao and G. Wang, *Curr. Opin. Green Sustainable Chem.*, 2022, **34**, 100589.

38 B. Jia, L. Li, C. Xue, J. Kang, L. Liu, T. Guo, Z. Wang, Q. Huang and S. Guo, *Adv. Mater.*, 2023, **35**, 2305587.
39 S. Sultan, H. Lee, S. Park, M. M. Kim, A. Yoon, H. Choi, T.-H. Kong, Y.-J. Koe, H.-S. Oh, Z. Lee, H. Kim, W. Kim and Y. Kwon, *Energy Environ. Sci.*, 2022, **15**, 2397–2409.
40 G. Kastlunger, L. Wang, N. Govindarajan, H. H. Heenen, S. Ringe, T. Jaramillo, C. Hahn and K. Chan, *ACS Catal.*, 2022, **12**, 4344–4357.
41 Y. Zhao, X. Chang, A. S. Malkani, X. Yang, L. Thompson, F. Jiao and B. Xu, *J. Am. Chem. Soc.*, 2020, **142**, 9735–9743.
42 C. M. Gunathunge, X. Li, J. Li, R. P. Hicks, V. J. Ovalle and M. M. Waegele, *J. Phys. Chem. C*, 2017, **121**, 12337–12344.
43 M. Moradzaman and G. Mul, *ChemElectroChem*, 2021, **8**, 1478–1485.
44 C. Liu, X. Zhang, J. Huang, M. Guan, M. Xu and Z. Gu, *ACS Catal.*, 2022, **12**, 15230–15240.
45 P. Li, J. Bi, J. Liu, Y. Wang, X. Kang, X. Sun, J. Zhang, Z. Liu, Q. Zhu and B. Han, *J. Am. Chem. Soc.*, 2023, **145**, 4675–4682.

Published on 15 de gener 2024. Downloaded on 31/5/2026 0:39:09.

This journal is © The Royal Society of Chemistry 2024